

# Zigzag edge states in graphene in the presence of in-plane electric field

A.A. Herasymchuk

*Department of Physics, Taras Shevchenko National University of Kyiv,  
64/13, Volodymyrska Street, Kyiv 01601, Ukraine*

S.G. Sharapov

*Bogolyubov Institute for Theoretical Physics, National Academy of Science of Ukraine,  
14-b Metrologichna Street, Kyiv, 03143, Ukraine and  
Kyiv Academic University, 03142 Kyiv, Ukraine*

V.P. Gusynin

*Bogolyubov Institute for Theoretical Physics, National Academy of Science of Ukraine,  
14-b Metrologichna Street, Kyiv, 03143, Ukraine*

(Dated: April 17, 2023)

The present study explores the edge states in a finite-width graphene ribbon and a semi-infinite geometry subject to a perpendicular magnetic field and an in-plane electric field, applied perpendicular to a zigzag edge. To accomplish this, a combination of analytic and numerical methods within the framework of low-energy effective theory is employed. Both the gapless and gapped Dirac fermions in graphene are considered. It is found that a surface mode localized at the zigzag edge remains dispersionless even in the presence of electric field. This is shown analytically by employing Darwin's expansion of the parabolic cylinder functions of large order and argument.

## I. INTRODUCTION

Graphene continues to be a playground for investigating a plethora of unusual electronic phenomena, making it a fascinating system for fundamental studies in condensed matter physics. The fact that graphene is two-dimensional material allows to access the regime when the confining potential at the edges of graphene nanoribbons is atomically sharp. The quantum Hall edge states in this case are defined by boundary conditions of vanishing electron wave functions at the crystal edges.

We recall that in the conventional experiments on two-dimensional semiconductors only the regime with electrostatically reconstructed edges is accessible. In this case the system lowers its energy by reconstructing the edge states into steps which produce alternating compressible and incompressible stripes [1]. Furthermore, imaging these edge states is difficult because they are buried inside the semiconductors.

Therefore graphene provides an opportunity to explore the real-space structure of the edge states by scanning probe techniques [2, 3] avoiding their electrostatic reconstruction. Other techniques of visualization of charge transport through Landau levels are also available. For example, one can rely on the scanning photocurrent microscopy [4] to use an engineered array of near-surface, atomic-sized quantum sensors [5] or apply high-resolution atomic force microscopy [6].

An additional opportunity provided by graphene is a mechanism for manipulating the transport channels by using an external in-plane Hall electric field. Theoretical exploration of this mechanism is based on description of graphene layer in crossed uniform electric and magnetic fields.

The behavior of electrons in crossed electric and

magnetic fields was studied by considering the  $3 + 1$ -dimensional Dirac equation. For example, it was shown that there are no relativistic corrections to the quantized Hall conductivity [7, 8].

After discovery of graphene an attention to  $2 + 1$ -relativistic fermions in crossed fields was brought because of the spectacular phenomenon of Landau level collapse. As the dimensionless parameter  $\beta = cE/(v_F H)$  reaches its critical value,  $|\beta_c| = 1$ , the Landau level staircase merges [9, 10]. Here  $H$  is a magnetic field  $H$  applied perpendicular to the sheet of graphene,  $E$  is an applied in-plane electric field  $E$ ,  $v_F$  is the Fermi velocity and CGS units are used. The observation of the Landau level collapse was reported in Refs. [11, 12].

The spectrum of an infinite graphene's sheet in presence of crossed uniform electric and magnetic fields was investigated analytically in Ref. [9] by means of a "Lorentz boost" transformation that eliminates the electric field and thus reduces the problem of finding spectrum to the known one. The same problem was addressed in Ref. [10] using algebraic methods. The influence of a Hall electric field on the Hall conductivity in graphene was analytically studied in Ref. [13] using the spectrum and wave functions found in Refs. [9, 10]. Another possibility to realize the Landau-level collapse would be by generating strain induced either pseudomagnetic or electric fields suggested in Refs. [14, 15], respectively (see also, for example, Refs. [16, 17] on a recent progress in curved spacetime Dirac equation approach for generation of these fields). The creation of pseudomagnetic field in graphene was proven experimentally in Ref. [18].

As the parameter  $\beta$  approaches the critical value, the large values of the involved wave vectors go beyond the range of applicability of long wave length approximation. Nevertheless, its validity was verified in Ref. [9] by per-

forming numerical computations on tight binding model for graphene lattices of a finite size with the current parallel to the zigzag edges. Still the Landau level collapse occurs in this case, yet at the lower value of  $\beta_c \simeq 0.9$ .

Furthermore, numerical computations on the finite lattice in Ref. [9] [see also Refs. [19, 20]] allow to explore the evolution of the edge states in the presence of electric field. One of the observations is that because of the tilt of the spectrum, the number of edge channels on the two sides of the zigzag ribbon becomes different, and current carrying channels appear in the middle of the stripe [20].

The ribbons with current along the armchair edges were considered in Ref. [19]. It is pointed out that the combined effect of both magnetic and electric fields breaks the symmetry between electronic and hole energy bands which is present when either magnetic or electric field is applied. This paves a way for creation valley filtering devices tunable by an in-plane electric field [21] (see also, e.g. Ref. [22]). Various ways of controlling the electron propagation in graphene nanostructures with magnetic and electric fields are discussed, for example, in Refs. [23–26].

In addition to the analytical studies of Landau levels in crossed fields [9, 10], Landau levels for ribbons and in semi-infinite geometries were also investigated using the low-energy model without electric field. The corresponding differential equation for the spectrum with the appropriate boundary conditions is treated analytically and then the eigenenergies are computed numerically by solving the transcendental equation for gapless [27–30] and gapped [31–33] graphene. A quantitative analytical description of the edge states within WKB approximation is developed in Ref. [34] basing on an effective Hamiltonian with a potential depending on the boundary conditions [27, 28].

On the other hand, the consideration of Landau levels in the crossed fields on the ribbons is limited to the numerical consideration of the lattice model [9, 19, 20]. The purpose of the present work is to extend the analytical study of graphene nanoribbons in the crossed magnetic and in-plane electric Hall field applied perpendicular to the ribbon edges.

The paper is organized as follows. In Sec. II, we introduce a low-energy model for a graphene ribbon with a zigzag edge subject to crossed magnetic and electric fields. A general solution of the differential equations describing graphene in terms of the parabolic cylinder Weber functions is obtained in Sec. III and the spectrum of an infinite graphene's sheet is reproduced. In Sec. IV, we present the spectra for a ribbon solving numerically the equations derived in Appendix A. In Sec. V, we present the spectra in a semi-infinite geometry and obtain the asymptotic solutions for these spectra for zero electric field in the bulk and near the edge. We also present an analytic consideration of the dispersionless mode specific for the zigzag edges. The details are provided in Appendix B. In the Conclusion (Sec. VI), we summarize the obtained results and discuss their possible experimental

observation.

## II. MODEL

To determine eigenenergy  $\mathcal{E}$  we consider the stationary Dirac equation

$$[\hbar v_F (-\alpha_1 i D_x - \alpha_2 i D_y) + \Delta \alpha_3 + V(\mathbf{r}) - \mathcal{E}] \Psi(\mathbf{r}) = 0, \quad (1)$$

which describes low-energy excitations in graphene. The  $4 \times 4$   $\alpha$ -matrices  $\alpha_i = \tau_3 \otimes \sigma_i$  and the Pauli matrices  $\tau_i, \sigma_i$  (as well as the  $2 \times 2$  unit matrices  $\tau_0, \sigma_0$ ) act on the valley ( $\mathbf{K}_\eta$  with  $\eta = \pm$ ) and sublattice ( $A, B$ ) indices, respectively, of the four component spinors  $\Psi^T = (\Psi_+^T, \Psi_-^T) = (\psi_{AK_+}, \psi_{BK_+}, \psi_{BK_-}, \psi_{AK_-})$ . This representation follows from a tight-binding model for graphene, see e.g. Ref. [35] and thus allows one to write down the appropriate boundary conditions for zigzag and armchair edges in the continuum model.

We consider both the massless Dirac-Weyl fermions in the pristine graphene and the massive Dirac fermions with the mass  $\Delta/v_F^2$ . Note that a global  $A/B$  sublattice asymmetry gap  $2\Delta \sim 350$  K can be introduced in graphene [36–39] when it is placed on top of hexagonal boron nitride (G/hBN) and the crystallographic axes of graphene and hBN are aligned.

The orbital effect of a perpendicular magnetic field  $\mathbf{H} = \nabla \times \mathbf{A}$  is included via the covariant spatial derivative  $D_j = \partial_j + (ie/\hbar c)A_j$  with  $j = x, y$  and  $-e < 0$ , while the potential  $V(\mathbf{r})$  corresponds to the static electric field  $e\mathbf{E} = \nabla V(\mathbf{r})$ . Since moderate values of magnetic field are considered, the Zeeman energy is small and neglected in this paper (see, e.g., Ref. [35]).

We consider the ribbons with the zigzag as shown in Fig. 1. The ribbons are subjected to the combination

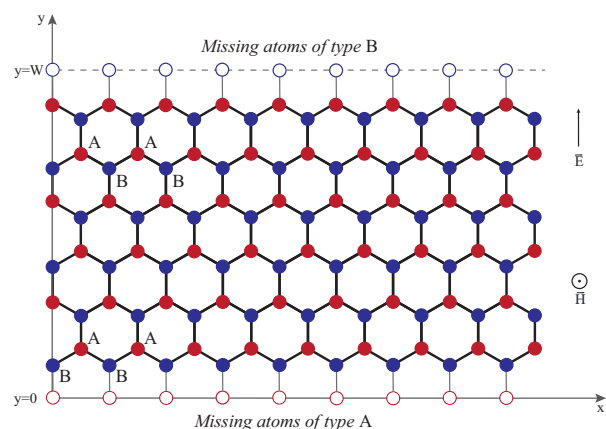


FIG. 1. The lattice structure of a finite width graphene ribbon with zigzag edge and the configuration of applied magnetic and electric fields.

of crossed uniform magnetic and electric fields. The magnetic field  $\mathbf{H}$  applied perpendicular to the plane of

graphene ribbon along the positive  $z$  axis, and in-plane electric field  $\mathbf{E}$  applied perpendicular to the ribbon edges.

The equation (1) splits into a pair of two independent Dirac equations for each  $\mathbf{K}_\eta$  point:

$$[-i\hbar v_F \eta (\sigma_1 D_x + \sigma_2 D_y) + \eta \Delta \sigma_3 + V(\mathbf{r}) - \mathcal{E}] \Psi_\eta(\mathbf{r}) = 0 \quad (2)$$

and as we will discuss below, the boundary conditions for the zigzag edges (7) also do not mix the corresponding wave functions.

One can see from Eq. (2) that having the solutions for  $\mathbf{K}_+$  point, the corresponding solutions for  $\mathbf{K}_-$  can be obtained by changing the signs of energy  $\mathcal{E}$  and electric field in  $V(\mathbf{r})$ . Finally, one should take into account that for the spinor  $\Psi_-$  the components of the spinor corresponding to  $A$  and  $B$  sublattices are exchanged as compared to  $\Psi_+$ .

A zigzag edge is parallel to the  $x$  direction as shown in Fig. 1. The in-plane electric field  $\mathbf{E}$  is applied in the  $y$  direction, so the potential  $V(\mathbf{r}) = eEy$ . The vector potential is taken in the Landau gauge,  $(A_x, A_y) = (-Hy, 0)$ , where  $H$  is the magnitude of a constant magnetic field orthogonal to the graphene plane.

Accordingly, the differential equations in Eq. (1) do not depend explicitly on the  $x$  coordinate. Therefore, the wave functions are plane waves in the  $x$  direction,

$$\begin{aligned} \psi_{A\mathbf{K}_+}(\mathbf{r}, k) &= \frac{e^{-ikx}}{\sqrt{2\pi l}} u_+(y, k), & \psi_{B\mathbf{K}_+}(\mathbf{r}, k) &= \frac{e^{-ikx}}{\sqrt{2\pi l}} v_+(y, k), \\ \psi_{A\mathbf{K}_-}(\mathbf{r}, k) &= \frac{e^{-ikx}}{\sqrt{2\pi l}} u_-(y, k), & \psi_{B\mathbf{K}_-}(\mathbf{r}, k) &= \frac{e^{-ikx}}{\sqrt{2\pi l}} v_-(y, k). \end{aligned} \quad (3)$$

The wave vector  $k$  measures the displacement from  $\mathbf{K}_\eta$  points. A particular choice of the coordinate system in Ref. [35] determines that  $\mathbf{K}_\pm = \pm(2\pi/a)(2/3, 0)$ , where  $a$  is the lattice constant. The maximum value of the wave vector  $k$  is limited by the boundaries of the first Brillouin zone.

Recall that the wave vector  $k$  determines the center of the electron orbit along the  $y$  direction,  $y_0 = -kl^2$ . Then, as we shall see below, for a system with a ribbon geometry, e.g.,  $0 \leq y \leq W$ , the condition that the peak of the wave function is inside the ribbon will be satisfied only for eigenstates with wave vectors  $k$  in a finite range,  $-W/l^2 \leq k \leq 0$ . This is known as the position – wave vector duality in the Landau gauge. Note that the values of the total wave vector for different  $\mathbf{K}_\eta$  valleys in the tight-binding calculation fall in different wave vectors domains, because  $K_{+x} \neq K_{-x}$ .

Substituting Eq. (3) in Eq. (2) we obtain the following system of equations for the  $\mathbf{K}_+$  point

$$\begin{pmatrix} \frac{eEy - \mathcal{E} + \Delta}{\hbar v_F} & -\partial_y - k - \frac{e}{\hbar c} Hy \\ \partial_y - k - \frac{e}{\hbar c} Hy & \frac{eEy - \mathcal{E} - \Delta}{\hbar v_F} \end{pmatrix} \psi_+ = 0, \quad (4)$$

where  $\psi_+^T = (u_+, v_+)$ . One can see that the envelope functions  $u_+(y, k)$  and  $v_+(y, k)$  ( $u_-(y, k)$  and  $v_-(y, k)$ )

depend only on a single dimensionless combination of the variables,  $\xi = y/l + kl$  with  $l = \sqrt{\hbar c/|eH|}$  being the magnetic length, so Eq. (4) acquires the form

$$\begin{pmatrix} \beta\xi - \epsilon + \delta & -i\partial_\xi - i\xi \\ -i\partial_\xi + i\xi & \beta\xi - \epsilon - \delta \end{pmatrix} \tilde{\psi}_+ = 0. \quad (5)$$

Here we introduced the notations

$$\beta = \frac{cE}{v_F H}, \quad \epsilon = \frac{l\mathcal{E}}{\hbar v_F} + l\beta k, \quad \delta = \frac{l\Delta}{\hbar v_F}. \quad (6)$$

Writing Eq. (5) we used the spinor  $\tilde{\psi}_+^T = (u_+, -iv_+)$ . This notation together with the opposite sign in  $\exp(-ikx)$  as compared to [31–33] allows us to unify the equations describing zigzag and armchair edges. The latter will be considered in a separate publication. Here we only remind that the dispersionless edge mode is absent in the case of the armchair edge.

The important dimensionless parameter  $\beta$  in Eq. (6) describes the strength of the electric field relative to the magnetic field. In this paper, we restrict ourselves to the  $|\beta| \leq 1$  case and do not consider pair creation regime.

To obtain the energy spectrum we need to supplement the differential equations for the envelope functions  $u_\pm(y, k)$  and  $v_\pm(y, k)$  with suitable boundary conditions. Such conditions can be derived from the tight-binding model [27, 28, 40, 41].

In the case of a graphene ribbon of a finite width in the  $y$  direction,  $0 \leq y \leq W$ , and with two zigzag edges parallel to the  $x$  direction, the  $A$  and  $B$  components of wave functions should vanish on the opposite edges:

$$y = 0 : \quad u_+(kl) = u_-(kl) = 0, \quad (7a)$$

$$y = W : \quad v_+(W/l + kl) = v_-(W/l + kl) = 0, \quad (7b)$$

see Fig. 1. Note that the case of the armchair edges is different, because in the tight-binding calculation the values of the total wave vector projected on the armchair edge direction coincide for the different  $\mathbf{K}_\eta$  valleys (see e.g. Ref. [34]). This allows valley admixing by the boundary condition.

### III. GENERAL SOLUTIONS

As mentioned in Introduction, the Dirac equation (2) for the massless case,  $\Delta = 0$  and infinite plane was solved in Refs. [9, 10]. Here we apply a different analytic approach for a finite system.

The main equation (5) can be rewritten in the following form

$$\partial_\xi \tilde{\psi}_+(\xi) = \left( \tilde{A} + \tilde{B}\xi \right) \tilde{\psi}_+(\xi) \quad (8)$$

where the  $2 \times 2$   $\xi$ -independent matrices  $\tilde{A}, \tilde{B}$  are, respectively,

$$\tilde{A} = \begin{pmatrix} 0 & i(\epsilon + \delta) \\ i(\epsilon - \delta) & 0 \end{pmatrix}, \quad \tilde{B} = \begin{pmatrix} 1 & -i\beta \\ -i\beta & -1 \end{pmatrix}. \quad (9)$$

Now we make the transformation  $\tilde{\psi}_+ = P\chi$  with the matrix  $P$  which diagonalizes the matrix  $\tilde{B}$ , where the matrix

$$P = \begin{pmatrix} i\gamma & i \\ 1 & \gamma \end{pmatrix}, \quad \gamma = \frac{\beta}{1 + \sqrt{1 - \beta^2}}. \quad (10)$$

Thus one transforms the system (8) to the form

$$\partial_\xi \chi(\xi) = (A + B\xi) \chi(\xi) \quad (11)$$

with

$$A = P^{-1} \tilde{A} P = \begin{pmatrix} -\frac{\beta\epsilon}{\sqrt{1-\beta^2}} & \delta - \frac{\epsilon}{\sqrt{1-\beta^2}} \\ \delta + \frac{\epsilon}{\sqrt{1-\beta^2}} & \frac{\beta\epsilon}{\sqrt{1-\beta^2}} \end{pmatrix}, \quad (12)$$

and

$$B = P^{-1} \tilde{B} P = \begin{pmatrix} -\sqrt{1-\beta^2} & 0 \\ 0 & \sqrt{1-\beta^2} \end{pmatrix}. \quad (13)$$

Note that while the present problem in the crossed uniform fields in the Cartesian coordinates is exactly solvable by diagonalizing the matrix  $B$ , the problem with the radial electric field [42] which involves three matrices  $\hat{A}/\rho + \hat{B} + \hat{C}\rho$  with  $\rho$  being the radial variable cannot be solved analytically.

Introducing a new variable  $\zeta = (1 - \beta^2)^{1/4} \xi + \beta\epsilon/(1 - \beta^2)^{3/4}$ , we rewrite Eq. (11) as follows

$$\partial_\zeta \chi(\zeta) = \begin{pmatrix} -\zeta & \sqrt{2}\kappa_- \\ \sqrt{2}\kappa_+ & \zeta \end{pmatrix} \chi(\zeta), \quad (14)$$

where the following notations are introduced

$$\kappa_\pm = \frac{\delta\sqrt{1-\beta^2} \pm \epsilon}{\sqrt{2}(1-\beta^2)^{3/4}}. \quad (15)$$

Then one can express the component  $\chi_1$  via  $\chi_2$ ,

$$\chi_1(\zeta) = \frac{\chi_2'(\zeta) - \zeta\chi_2(\zeta)}{\sqrt{2}\kappa_+}, \quad (16)$$

and obtain the following equation for  $\chi_2$ :

$$\chi_2''(\zeta) - (1 + \zeta^2 + 2\kappa_- \kappa_+) \chi_2(\zeta) = 0. \quad (17)$$

Here prime denotes a differentiation over  $\zeta$ .

The general solution of the last equation can be written in terms of the parabolic cylinder (Weber) functions  $U(a, x)$  and  $V(a, x)$  [43]

$$\chi_2(\zeta) = C_1 U\left(a, \sqrt{2}\zeta\right) + C_2 V\left(a, \sqrt{2}\zeta\right) \quad (18)$$

with

$$a = \frac{1}{2} + \kappa_+ \kappa_- = \frac{1}{2} + \frac{\delta^2(1-\beta^2) - \epsilon^2}{2(1-\beta^2)^{3/2}}. \quad (19)$$

and  $C_{1,2}$  being the integration constants. Accordingly, using the recurrence relations (19.6.2) and (19.6.5) from [43]:

$$\begin{aligned} U'(a, x) - \frac{x}{2}U(a, x) + U(a-1, x) &= 0, \\ V'(a, x) - \frac{x}{2}V(a, x) - \left(a - \frac{1}{2}\right)V(a-1, x) &= 0 \end{aligned} \quad (20)$$

we obtain from Eq. (16) the expression for  $\chi_1$  component

$$\chi_1(\zeta) = -\frac{1}{\kappa_+} \left[ C_1 U\left(a-1, \sqrt{2}\zeta\right) - C_2 \left(a - \frac{1}{2}\right) V\left(a-1, \sqrt{2}\zeta\right) \right]. \quad (21)$$

One can notice from the definition of  $\zeta$  that for a finite electric field, the electron- and hole-like solutions become asymmetric.

Finally, one should return to the original spinor components for the sublattices,  $\tilde{\psi}_+ = P\chi$  (see Appendix A). The representation of the solution Eqs. (A1) and (A2) (see also Eqs. (21) and (18)) in terms of the Weber parabolic cylinder functions  $U(a, x)$  and  $V(a, x)$  is particularly convenient because their Wronskian  $W\{U, V\} = \sqrt{2/\pi}$  [43] is independent of the parameters.

Another advantage of utilizing these functions is that in an infinite system without boundaries, the normalizable wave functions contain only the parabolic cylinder  $U(a, x)$  functions. This is because the cylinder functions  $V(a, x)$  diverge exponentially for both positive and negative  $x$ , as shown by the asymptotics (A3b) and (A5b), which necessitates  $C_2$  to be equal to zero. As one can see from Eq. (A3a) the remaining  $U(a, x)$  functions are bound at  $x \rightarrow +\infty$ . Furthermore, it follows from Eq. (A5b) that the condition of their finiteness at  $x \rightarrow -\infty$  requires that  $a = -n - 1/2$  with  $n$  being a non-negative integer, viz.

$$\epsilon_n = (1 - \beta^2)^{1/2} \begin{cases} -\eta\delta \operatorname{sgn}(eH), & n = 0, \\ \pm\sqrt{2n(1 - \beta^2)^{1/2} + \delta^2}, & n = 1, 2, \dots \end{cases} \quad (22)$$

Thus we recover the result of Refs. [9, 10] generalized for a finite  $\Delta$  case (see Ref. [44] and recent works [42, 45]):

$$\begin{aligned} \mathcal{E}_n &= \mathcal{E}_n^* - \hbar k \frac{cE}{H}, \\ \mathcal{E}_n^* &= (1 - \beta^2)^{1/2} \\ &\times \begin{cases} -\eta\Delta, & n = 0, \\ \pm\sqrt{\frac{2n\hbar v_F^2 eH}{c}(1 - \beta^2)^{1/2} + \Delta^2}, & n = 1, 2, \dots \end{cases} \end{aligned} \quad (23)$$

Here and in what follows we assume that  $H > 0$ . Obviously the collapse of Landau levels occurs as  $|\beta|$  approaches 1.

#### IV. ZIGZAG EDGE STATES FOR A RIBBON

To comprehend a link between the existing computations on the lattice and the considered here continuum model we begin with numerical solution of the equations (A6) and (A8) derived in Appendix A. They determine dimensionless energies  $\epsilon_\alpha = \epsilon_n(kl, W/l)$  as functions of quantum numbers  $\alpha \equiv (n, k)$  and the ratio  $W/l$  for the  $\mathbf{K}_+$  and  $\mathbf{K}_-$  valleys, respectively. To return to the total energy  $\mathcal{E}$  (or its dimensionless analog  $l\mathcal{E}/(\hbar v_F)$ ) one should use Eq. (6) to restore its linear in  $k$  part.

##### A. The gapless case, $\Delta = 0$

The corresponding spectra for  $\Delta = 0$  case are computed numerically and presented in Fig. 2. The panels (a), (b) show the results for zero and the panels (c), (d) for a finite ( $\beta = 0.1$ ) electric field. Since the wave vec-

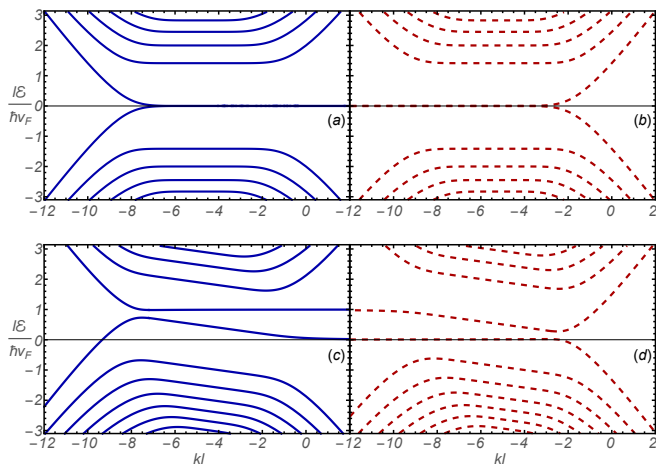


FIG. 2. The energy spectra  $l\mathcal{E}(k)/(\hbar v_F)$  of the first few Landau levels of the ribbon of widths  $W = 10l$  for the gapless,  $\Delta = 0$  case. Panels (a) and (b) show the results for  $\beta = 0$  and (c) and (d) for  $\beta = 0.1$ , respectively. The solutions for the  $\mathbf{K}_+$  valley are shown in panels (a) and (c) by the solid (blue) lines, the solutions for the  $\mathbf{K}_-$  valley in panels (b) and (d) by the dashed (red) lines.

tor  $k$  is counted from  $K_{\pm x}$  the spectra for both valleys fell on the same range of the wave vectors as compared to the solutions of the lattice model [9, 19, 20], where the wave vector includes the value  $K_{\pm x}$ . In our case the edges correspond to the values  $kl = -10$  and  $kl = 0$  for both valleys, but to facilitate the comparison we showed the results for the  $\mathbf{K}_+$  and  $\mathbf{K}_-$  valleys side by side. One finds that the results presented in Fig. 2 are in agreement with the calculations done for the lattice model in a finite electric field [9, 20] (notice the opposite sign of  $k$ ).

In Fig. 2 (a), (b) we observe the dispersionless Landau levels in the bulk of the ribbon. The  $n \neq 0$  Landau levels are dispersing independently near the edges for each valley, while for the lowest  $n = 0$  Landau level there is

a dispersionless part of the spectrum branch that unites both valleys together. These dispersionless surface states localized at the boundaries [27, 28, 41, 46] and  $n = 0$  Landau level form the degenerate states.

On the contrary, Fig. 2 (c), (d) show that the degeneracy is lifted by an applied electric field [9]. All Landau levels including the lowest one develop a linear  $k$  dispersion with the slope proportional to the electric field, whereas only the surface states remain dispersionless.

##### B. The gapped case

The corresponding spectra for a finite  $\Delta$  case are computed numerically and presented in Fig. 3. The corre-

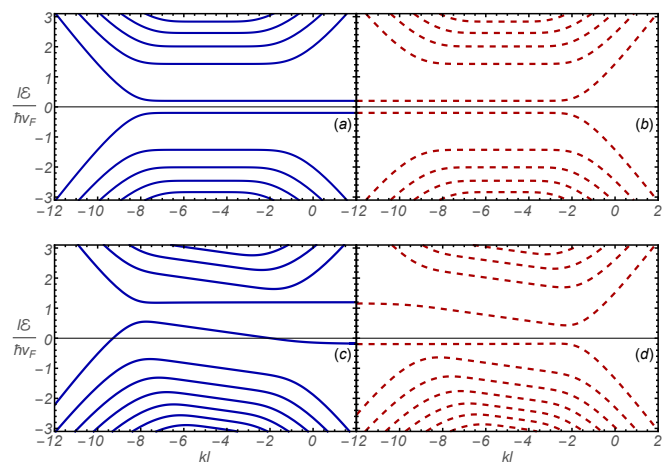


FIG. 3. The energy spectra  $l\mathcal{E}(k)/(\hbar v_F)$  of the first few Landau levels of the ribbon of widths  $W = 10l$  for the gapped,  $\delta = 0.2$  case. The panels (a), (b), (c) and (d) are for the same valleys and values of  $\beta$  as in Fig. 2.

sponding numerical solution shown in Figs. 3 (a) and (b) is in agreement with the results presented in Refs. [33] for zero electric field. The gap  $\Delta$  considered in the present work corresponds to the parity breaking and the time reversal symmetry conserving gap  $\tilde{\Delta}$  in the notation of [31–33].

The presence of the mass gap results in the absence of the gapless edge states, the degeneracy of the  $n = 0$  level is lifted. The degeneracy of the surface modes is also lifted, yet they remain dispersionless with the energies  $\sim \pm\Delta$ .

In the presence of an electric field [see Figs. 3 (c) and (d)] all Landau levels acquire linear  $k$  dispersion, but the surface modes remain dispersionless. Furthermore, while for the  $\Delta = 0$  case the linearly dispersing part of the  $n = 0$  level has the same energy, for a finite  $\Delta$  this degeneracy is lifted as for the  $\beta = 0$  case.

To study the discussed features by analytic methods we need to simplify the problem by considering the semi-infinite geometry.

## V. ZIGZAG EDGE IN SEMI-INFINITE GEOMETRY

On a half-plane, normalizable wave functions are also given in terms of only  $U(a, x)$  function which as mentioned above falls off exponentially as  $x \rightarrow \infty$ , while the function  $V(a, z)$  is growing exponentially in both directions  $x \rightarrow \pm\infty$ . Therefore, we must take again  $C_2 = 0$ . Yet, in contrast to the case of an infinite plane, on a half-plane, there is no restriction for the parameter  $a$  to be a negative half-integer [see the discussion above Eq. (22)].

The zigzag boundary conditions (7b) at  $y = W \rightarrow \infty$  are automatically satisfied due to the asymptotic (A3a). It follows from the remaining boundary conditions (7a) at  $y = 0$  that the term with  $C_1$  in Eq. (A1) has to be zero. The latter condition produces the following equation for the spectrum for the  $\mathbf{K}_+$  valley:

$$\gamma U(a - 1, \sqrt{2}\zeta(0)) - \kappa_+ U(a, \sqrt{2}\zeta(0)) = 0. \quad (24)$$

Using the asymptotics Eq. (A3) one can verify that Eq. (24) also follows from Eq. (A6) in the limit  $W \rightarrow \infty$ .

To write down the corresponding equation for the spectrum for the  $\mathbf{K}_-$  valley we use the prescriptions described below Eq. (2). They imply that  $\epsilon \rightarrow -\epsilon$ ,  $\beta \rightarrow -\beta$  and  $\psi_1 \leftrightarrow \psi_2$ , so that we arrive at the following equation

$$U(a - 1, \sqrt{2}\zeta(0)) + \gamma\kappa_- U(a, \sqrt{2}\zeta(0)) = 0. \quad (25)$$

Eqs. (24) and (25) determine dimensionless energies  $\epsilon_\alpha = \epsilon_n(kl)$  as functions of quantum numbers  $\alpha \equiv (n, k)$ . To return to the total energy  $\mathcal{E}$  (or its dimensionless analog  $l\mathcal{E}/(\hbar v_F)$ ) one should use Eq. (6) to restore its linear in  $k$  part.

The corresponding spectra are computed numerically and presented for the gapless and gapped cases in Figs. 4 and 5, respectively. In contrast to Figs. 2 and 3 where we showed the  $\mathbf{K}_+$  and  $\mathbf{K}_-$  valleys on separate panels, here we superimpose both valleys on the same panel to allow a direct comparison of the corresponding energy levels. This is possible, because in the continuum model the wave vector  $k$  is counted from  $K_{\pm x}$  values. The negative values of  $k$  correspond to the bulk, while the edge is at  $k = 0$ .

Since a half-plane geometry is considered, for a finite  $\beta$  there is an unbound linear growth of the dispersion curves as  $kl \rightarrow -\infty$ . The presence of the other edge at  $y = W$  modifies this behavior. The hole-like levels including the blue line (the  $\mathbf{K}_+$  solution) that goes to zero for  $kl \rightarrow \infty$  would go downward, while the electron-like levels go upward. Furthermore, the degeneracy of the solutions for the  $\mathbf{K}_+$  and  $\mathbf{K}_-$  valleys would be lifted near the other edge as one can see in Figs. 2 and 3.

The only curve which remains dispersionless as  $kl \rightarrow -\infty$  even in the ribbon geometry is the zero energy lower branch of the  $\mathbf{K}_-$  valley spectrum that corresponds to the surface states mentioned in Sec. IV A. The second edge of the ribbon supports a second dispersionless mode which

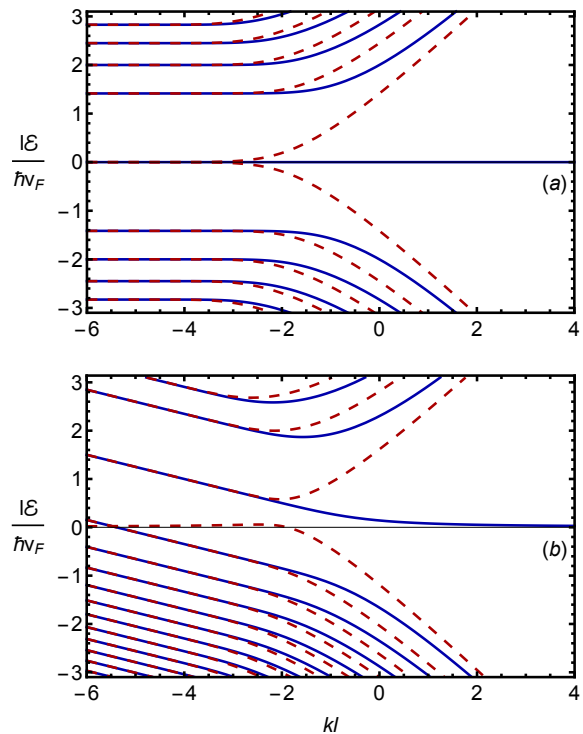


FIG. 4. The energy spectra  $l\mathcal{E}(k)/(\hbar v_F)$  of the first few Landau levels near a zigzag edge of graphene for the gapless,  $\Delta = 0$  case. The solutions for the  $\mathbf{K}_+$  and  $\mathbf{K}_-$  valleys are shown by the solid (blue) and dashed (red) lines, respectively. (a)  $\beta = 0$ ; (b)  $\beta = 0.25$

is absent in a half-plane geometry. The surface state in the semi-infinite geometry will be discussed in Sec. V B.

### A. Zero electric field limit

In the absence of electric field,  $\beta = \gamma = 0$  and  $a = [1 + \delta^2 - \epsilon^2]/2$ , so Eqs. (24) and (25) for the spectra in the  $\mathbf{K}_\pm$  valleys are in agreement with the equations studied in Refs. [31, 32]

$$(\delta + \epsilon)U(a, \sqrt{2}kl) = 0, \quad U(a - 1, \sqrt{2}kl) = 0. \quad (26)$$

The corresponding numerical solutions shown in Figs. 4 (a) and 5 (a) are in agreement with the results presented in Refs. [27, 28, 31, 32].

It is known that the zigzag edge hosts a band of dispersionless zero-energy states localized at the edge even in the absence of magnetic and electric fields [27, 28, 41, 46].

In the presence of a magnetic field, the lowest  $n = 0$  Landau level coexists with this surface state and behaves rather differently for the two valleys. As discussed in [28, 29], the lowest Landau level for the  $\mathbf{K}_+$  valley near the edge transforms into the surface mode [see the blue straight line in Fig. 4 (a)]. For the  $\mathbf{K}_-$  valley the lowest Landau level and the surface state mix, producing two

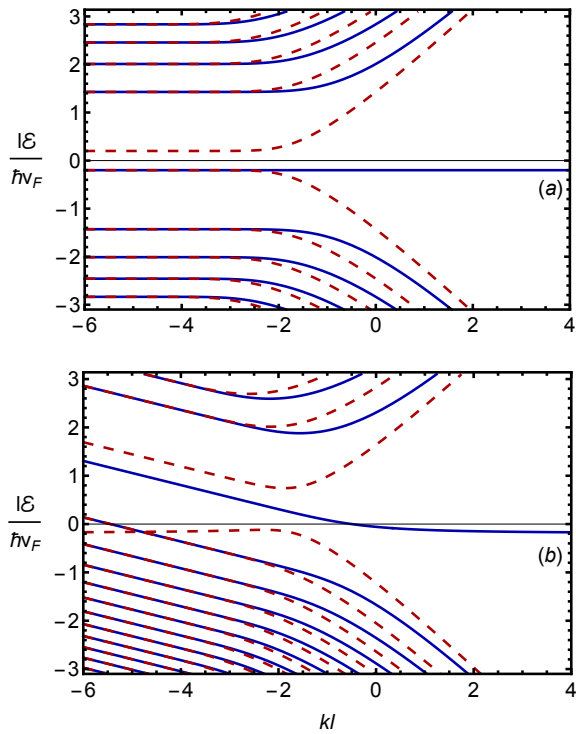


FIG. 5. The energy spectra  $\mathcal{E}(k)/(\hbar v_F)$  of the first few Landau levels near a zigzag edge of graphene for the gapped,  $\delta = 0.2$  case. The panels (a) and (b) are for the same values of  $\beta$  as in Fig. 4.

dispersing edge modes as can be seen from the behavior of the red dashed lines in Fig. 4 (a).

It is possible to find out the approximate solutions of Eqs. (26) in the vicinity of the  $y = 0$  edge and for the bulk. The derivation follows along the lines of the corresponding derivation for the Schrödinger equation [47, 48]. First of all one can verify that the dispersionless solution  $\mathcal{E}_0 = -\Delta$  of the first equation in Eqs. (26) for the  $\mathbf{K}_+$  valley indeed satisfies the original system (14).

Depending on the relationship between the  $y$  coordinate of the center of the electron cyclotron orbit,  $y_0 = -kl^2$ , and the magnetic length  $l$  one can obtain two types of the asymptotic solutions of Eqs. (26).

For electrons near the boundary,  $y_0 \ll l$ , Eqs. (26) are solved by expanding the function  $U(a, z)$  in the argument  $z$  (see Eqs. (19.3.5) in [43]). In the first order in  $z$  we obtain the following equation  $\Gamma(1/4 + a/2)\Gamma^{-1}(3/4 + a/2) = \sqrt{2}z$  for the  $\mathbf{K}_+$  valley, while for the  $\mathbf{K}_-$  valley  $a \rightarrow a - 1$ . Exactly at the edge for  $z = -\sqrt{2}y_0 = 0$  the eigenenergies are determined by the poles of the gamma function  $\Gamma(z)$  in the denominator at  $z = -n$  with  $n = 0, 1, 2, \dots$ . These eigenvalues do not depend of  $y_0$ . Then we use the expansion  $\Gamma^{-1}(-n - \alpha) \simeq (-1)^n \Gamma(n + 1)(-\alpha)$  in order to obtain correction  $\alpha$  to these eigenenergies dependent on  $y_0$ .

For the bulk electrons,  $y_0 \gg l$ , the argument of the parabolic functions is large and negative, so that one uses firstly the relationship (A4a) which brings in the gamma

function  $\Gamma(1/2 + a)$  in the denominator. Then after using the asymptotic expressions (A3) essentially the same procedure as in the previous case is applied. As the result we obtain the following expressions for the  $\mathbf{K}_+$  valley

$$\epsilon_{+,n}^2 - \delta^2 = \begin{cases} 2n + \frac{2^n}{\sqrt{\pi(n-1)!}} \left(\frac{y_0}{l}\right)^{2n-1} e^{-y_0^2/l^2}, & y_0 \gg l, \\ 4n \left[1 - \frac{\Gamma(n+1/2)}{\pi n!} \frac{2y_0}{l}\right], & y_0 \ll l, \end{cases} \quad (27)$$

with  $n = 1, 2, \dots$  and for the  $\mathbf{K}_-$  valley

$$\epsilon_{-,n}^2 - \delta^2 = \begin{cases} 2n + \frac{2^{n+1}}{\sqrt{\pi n!}} \left(\frac{y_0}{l}\right)^{2n+1} e^{-y_0^2/l^2}, & y_0 \gg l, \\ 2(2n + 1) \left[1 - \frac{\Gamma(n+1/2)}{\pi n!} \frac{2y_0}{l}\right], & y_0 \ll l, \end{cases} \quad (28)$$

with  $n = 0, 1, 2, \dots$ . The level  $\epsilon_{-,0} \approx -\delta$  is related to the surface mode and it disappears when the edge is moved to infinity, similarly to the disappearance of another surface mode when one goes from the ribbon to a half-plane geometry. Thus the combined spectrum for both  $\mathbf{K}_\pm$  valleys reduces the one to given by Eq. (22) with  $\beta = 0$ .

By studying the spectra of the edge and bulk regions, we can observe an interesting property: for the  $\mathbf{K}_+$  valley, we have  $\epsilon_{+,n}(y_0 = 0) = \epsilon_{+,2n}(y_0 \gg l)$  with  $n > 0$ , and for the  $\mathbf{K}_-$  valley, we have  $\epsilon_{-,n}(y_0 = 0) = \epsilon_{-,2n+1}(y_0 \gg l)$  with  $n \geq 0$  [29, 34]. This feature of the spectra can be traced back to the character of the spectrum for the harmonic oscillator with reflecting wall at the minimum of potential (see the Problem 2.5 in Ref. [49]). The difference between the valleys is caused by the difference of the first arguments of  $U$  in Eqs. (26). When the opposite edge is also considered, these properties of the spectra for the  $\mathbf{K}_+$  and  $\mathbf{K}_-$  valleys are interchanged.

## B. The lowest Landau level and surface mode in a finite electric field

As discussed at the end of Sec. IV A, the electric field lifts the degeneracy of the  $n = 0$  Landau level and the dispersionless state. Indeed, in Fig. 4 (b) one observes splitting of the two red (dashed) curves for the  $\mathbf{K}_-$  valley that merge to zero energy in Fig. 4 (a) as  $kl \rightarrow -\infty$ . The upper curve corresponds to the dispersing  $n = 0$  level, while the lower curve is related to the dispersionless surface state. As we saw in the case of the ribbon shown Fig. 2 (c) and (d) in the  $\mathbf{K}_+$  valley this state evolves in the dispersing lowest  $n = 0$  Landau level whose energy decreases as  $kl \rightarrow -\infty$ . In a half-plane geometry the corresponding blue curve increases linearly as  $kl \rightarrow -\infty$ .

It is interesting to investigate the origin of the dispersionless state. Indeed, in our approach all branches of the spectrum are obtained from Eq. (6), viz.  $l\mathcal{E}/(\hbar v_F) = \epsilon - \beta kl$ . This implies that the linear dispersion of the Landau levels in the bulk is related to the  $-\beta kl$  ( $-\hbar k E/H$  in the dimensional units) term, while the dispersionless mode has to emerge from a delicate cancelation with the

$\epsilon$  term that should show the same dependence on  $kl$ . By using the expansion of parabolic cylinder functions of large order and argument as developed by Darwin [43], Appendix B demonstrates that a solution exists for the mode where  $\epsilon \sim \beta lk$  as  $kl \rightarrow -\infty$ .

Furthermore, one can show that there is also a similar surface mode solution in the  $\mathbf{K}_+$  valley which shows the same behavior as  $kl \rightarrow \infty$ .

For the  $\Delta = 0$  and finite  $\beta$  the dispersive parts of the curves corresponding to the  $n = 0$  level for the  $\mathbf{K}_+$  and  $\mathbf{K}_-$  valleys have the same energy [see Fig. 4 (b)]. As shown in Fig. 5 (b), for a finite  $\Delta$  this degeneracy is lifted as for the  $\beta = 0$  case. The dispersionless mode in the gapped case tends to  $\sim -\Delta$  value.

### C. Landau levels with $n \neq 0$ in a finite electric field

The behaviour of the  $n \neq 0$  Landau levels is similar for  $\beta = 0$  and finite  $\beta$ , viz. there are two branches of the edge states, one for each valley. These states are degenerate in the bulk and split near the edge. An increase in the electric field deforms the spectrum in two ways: firstly, the familiar linear term  $\hbar kE/H$ , which is present in nonrelativistic systems, appears; and secondly, the energy levels themselves merge as  $|\beta|$  approaches 1. Both these effects are indeed observed for the computations done for the larger values of  $\beta$  than shown in Figs. 4 (b) and 5 (b). The second feature reflects the Landau level collapse.

## VI. CONCLUSION

We conducted both analytical and numerical studies on the edge states of a graphene ribbon with finite width and semi-infinite geometry utilizing low-energy theory in the presence of the crossed magnetic and electric fields. Our findings are consistent with numerical calculations performed on a lattice. When an electric field is present, all Landau levels exhibit linear wave vector dispersion, except for surface modes that remain dispersionless. We devoted special attention to the analytical study of these states and demonstrated that they can be obtained using Darwin's expansion of the parabolic cylinder functions of large order and argument.

The existence of states localized near the zigzag edges of a graphene ribbon in the absence of a magnetic field was confirmed by STS measurements [50]. More recently, the signatures of these states were observed in magneto-transport measurements [51]. Extending these measurements to cases where an electric field is applied to the ribbon would be useful.

## ACKNOWLEDGMENTS

We would like to thank the Armed Forces of Ukraine for providing security to perform this work. The authors acknowledge a support by the National Research Foundation of Ukraine grant (2020.02/0051) "Topological phases of matter and excitations in Dirac materials, Josephson junctions and magnets". We would like to thank O.V. Bugaiko for participating in this work at its initial stage. We would like to express our gratitude to I.A. Shovkovy for insightful discussions on numerical methods.

### Appendix A: Explicit form of the solution and equations for eigenenergies

The explicit form of the general solution for the components of the spinor  $\tilde{\chi}$  reads

$$\begin{aligned} \tilde{\psi}_{+1}(\zeta) = & iC_{+1} \left[ \gamma U(a-1, \sqrt{2}\zeta) - \kappa_+ U(a, \sqrt{2}\zeta) \right] \\ & + iC_{+2} \left[ \gamma V(a-1, \sqrt{2}\zeta) + \frac{\kappa_+}{a-1/2} V(a, \sqrt{2}\zeta) \right], \end{aligned} \quad (\text{A1})$$

$$\begin{aligned} \tilde{\psi}_{+2}(\zeta) = & C_{+1} \left[ U(a-1, \sqrt{2}\zeta) - \gamma \kappa_+ U(a, \sqrt{2}\zeta) \right] \\ & + C_{+2} \left[ V(a-1, \sqrt{2}\zeta) + \frac{\gamma \kappa_+}{a-1/2} V(a, \sqrt{2}\zeta) \right], \end{aligned} \quad (\text{A2})$$

where for the convenience of further analysis we redefined the integration constants  $C_{1,2}$  in Eqs. (21) and (18). Writing Eqs. (A1) and (A2) we used  $\kappa_+$ ,  $a$  and  $\gamma$  defined by Eqs. (15), (19) and (10), respectively.

The asymptotic behavior of the functions  $U(a, x)$  and  $V(a, x)$  for the large positive  $x$  is the following (see Eqs. (19.8.1) and (19.8.2) from [43]):

$$U(a, x \rightarrow \infty) \simeq e^{-\frac{x^2}{4}} x^{-a-\frac{1}{2}} \left[ 1 + O\left(\frac{1}{x^2}\right) \right], \quad (\text{A3a})$$

$$V(a, x \rightarrow \infty) \simeq \sqrt{\frac{2}{\pi}} e^{\frac{x^2}{4}} x^{a-\frac{1}{2}} \left[ 1 + O\left(\frac{1}{x^2}\right) \right]. \quad (\text{A3b})$$

To derive asymptotics of the functions  $U(a, x)$ ,  $V(a, x)$  for large negative  $x$  we use Eqs. (19.4.2), (19.4.3) from [43] rewritten as follows

$$U(a, -x) = \frac{\pi}{\Gamma\left(\frac{1}{2} + a\right)} V(a, x) - \sin \pi a U(a, x), \quad (\text{A4a})$$

$$V(a, -x) = \sin \pi a V(a, x) + \frac{1}{\pi} \Gamma\left(\frac{1}{2} + a\right) \cos^2 \pi a U(a, x) \quad (\text{A4b})$$



and obtain as  $x \rightarrow \infty$ :

$$U(a, -x) \simeq \frac{\sqrt{2\pi}}{\Gamma\left(\frac{1}{2} + a\right)} e^{\frac{x^2}{4}} x^{a-\frac{1}{2}} \left[1 + O\left(\frac{1}{x^2}\right)\right], \quad (\text{A5a})$$

$$V(a, -x) \simeq \sqrt{\frac{2}{\pi}} \sin(\pi a) e^{\frac{x^2}{4}} x^{a-\frac{1}{2}} \left[1 + O\left(\frac{1}{x^2}\right)\right]. \quad (\text{A5b})$$

It follows from the zigzag boundary conditions (7) for the  $\mathbf{K}_+$  valley that the spectrum is determined by the following transcendental secular equation

$$\begin{aligned} & \left[ U(a-1, \sqrt{2}\zeta(W)) - \kappa_+ \gamma U(a, \sqrt{2}\zeta(W)) \right] \\ & \times \left[ \gamma V(a-1, \sqrt{2}\zeta(0)) + \frac{\kappa_+}{a-1/2} V(a, \sqrt{2}\zeta(0)) \right] \\ & = \left[ V(a-1, \sqrt{2}\zeta(W)) + \frac{\kappa_+ \gamma}{a-1/2} V(a, \sqrt{2}\zeta(W)) \right] \\ & \times \left[ \gamma U(a-1, \sqrt{2}\zeta(0)) - \kappa_+ U(a, \sqrt{2}\zeta(0)) \right], \end{aligned} \quad (\text{A6})$$

where

$$\begin{aligned} \zeta(0) \equiv \zeta(y=0) &= (1-\beta^2)^{1/4} kl + \frac{\beta\epsilon}{(1-\beta^2)^{3/4}}, \\ \zeta(W) \equiv \zeta(y=W) &= (1-\beta^2)^{1/4} \left( \frac{W}{l} + kl \right) \\ &+ \frac{\beta\epsilon}{(1-\beta^2)^{3/4}}. \end{aligned} \quad (\text{A7})$$

Recall also that  $\kappa_{\pm}$  and  $a$  depend on  $\epsilon$ . Using the prescriptions described above Eq. (25) one can write the corresponding secular equation for the spectrum for the  $\mathbf{K}_-$  valley:

$$\begin{aligned} & \left[ U(a-1, \sqrt{2}\zeta(0)) + \gamma \kappa_- U(a, \sqrt{2}\zeta(0)) \right] \\ & \times \left[ \gamma V(a-1, \sqrt{2}\zeta(W)) - \frac{\kappa_-}{a-\frac{1}{2}} U(a, \sqrt{2}\zeta(0)) \right] \\ & = \left[ \gamma U(a-1, \sqrt{2}\zeta(W)) + \kappa_- U(a, \sqrt{2}\zeta(W)) \right] \\ & \times \left[ V(a-1, \sqrt{2}\zeta(0)) - \frac{\gamma \kappa_-}{a-\frac{1}{2}} V(a, \sqrt{2}\zeta(0)) \right]. \end{aligned} \quad (\text{A8})$$

## Appendix B: Solution for the dispersionless mode at the $\mathbf{K}_-$ valley

We seek for a linear  $\epsilon \simeq Akl$  solution of Eq. (25) in the limit  $kl \rightarrow -\infty$ . It is convenient to rewrite this equation introducing the following notations  $\mathbf{a} \equiv a - 1/2 = \kappa_+ \kappa_-$  and  $x \equiv -\sqrt{2}\zeta(0) \rightarrow \infty$ :

$$U(\mathbf{a} - 1/2, -x) + \gamma \kappa_- U(\mathbf{a} + 1/2, -x) = 0. \quad (\text{B1})$$

Similarly to the derivation of the asymptotic solutions (27) and (28) for the  $y_0 \gg l$  case when the argument of

the parabolic functions is large and negative, one uses firstly the relationship (A4a) written in the following form

$$U(a, -x) = \Gamma(1/2 - a) \cos \pi a V(a, x) - \sin \pi a U(a, x). \quad (\text{B2})$$

However, in contrast to the abovementioned case of Eqs. (27) and (28) for  $y_0 \gg l$ , one cannot rely on the asymptotic expansions (A3), because the argument  $a$  of the parabolic functions also goes to  $-\infty$ .

Thus one has to use another expansion of the parabolic functions applicable for  $a < 0$ ,  $x \rightarrow +\infty$  and  $x^2 + 4a \rightarrow \infty$ . This case corresponds to the Darwin's expansion given by Eqs. (19.10.6) and (19.10.7) from [43]:

$$U(a, x) = \frac{\sqrt{\Gamma(1/2 - a)}}{(2\pi)^{1/4}} \exp[-\theta(a, x) + v(a, x)], \quad (\text{B3a})$$

$$V(a, x) = \frac{2}{(2\pi)^{1/4} \sqrt{\Gamma(1/2 - a)}} \exp[\theta(a, x) + v(a, -x)], \quad (\text{B3b})$$

where

$$\theta(a, x) = \frac{1}{4} x X(a) + a \ln \frac{x + X(a)}{2\sqrt{|a|}}, \quad (\text{B4})$$

$$v(a, x) \sim -\frac{1}{2} \ln X(a) + \sum_{s=1} (-1)^s \frac{d_{3s}}{X^{3s}(a)}, \quad (\text{B5})$$

with  $X(a) = \sqrt{x^2 - 4|a|}$ , and the coefficients  $d_{3s}$  are given in Eq. (19.10.13) in [43]. We are interested in the case  $X(a) \gg 1$ , so the terms with  $d_{3s}$  can be neglected. Furthermore, the functions  $U(\mathbf{a} \pm 1/2, x)$  that contain the decaying exponents  $\exp[-\theta(\mathbf{a} \pm 1/2, x)]$  in the  $x \rightarrow \infty$  limit may also be neglected, so that we are left with the following asymptotic expressions

$$\begin{aligned} U(\mathbf{a} - 1/2, -x) &= \\ & \frac{2 \sin \pi \mathbf{a} \sqrt{\Gamma(1 - \mathbf{a})}}{(2\pi)^{1/4}} X^{-1/2}(\mathbf{a} - 1/2, x) e^{\theta(\mathbf{a} - 1/2, x)}, \\ U(\mathbf{a} + 1/2, -x) &= \\ & - \frac{2 \sin \pi \mathbf{a} \sqrt{\Gamma(-\mathbf{a})}}{(2\pi)^{1/4}} X^{-1/2}(\mathbf{a} + 1/2, x) e^{\theta(\mathbf{a} + 1/2, x)} \end{aligned} \quad (\text{B6})$$

that has to be substituted into Eq. (B1). For  $|a| \gg 1$  the functions  $X^{-1/2}(\mathbf{a} + \lambda, x)$  and  $\theta(\mathbf{a} + \lambda, x)$  with  $\lambda = \pm 1/2$  can be expanded as follows

$$\begin{aligned} X^{-1/2}(\mathbf{a} + \lambda) &= X^{-1/2}(\mathbf{a}) - \frac{\lambda}{X^{5/2}(\mathbf{a})}, \\ \theta(\mathbf{a} + \lambda) &= \theta(\mathbf{a}) + \lambda \ln \frac{x + X(\mathbf{a})}{2\sqrt{-a}} + O\left(\frac{x}{\mathbf{a}X(\mathbf{a})}\right). \end{aligned} \quad (\text{B7})$$

To rewrite the final equation that relates  $\epsilon$  and  $kl$  in the considered limit in the most elucidating form, we introduce the new notations  $\mathbf{a} = -\mu^2/2$  and  $x = \mu t \sqrt{2}$ .

Then using Eq. (19) and the value  $\zeta(0)$  given by Eq. (A7) we obtain that

$$\mu = \frac{|\epsilon|}{(1 - \beta^2)^{3/4}}, \quad t = (1 - \beta^2) \frac{kl}{\epsilon} + \beta. \quad (\text{B8})$$

Then one can see that

$$\begin{aligned} \ln \frac{x + X(\mathbf{a})}{2\sqrt{-\mathbf{a}}} &= \ln(t + \sqrt{t^2 - 1}), \\ \theta(\mathbf{a}, x) &= \frac{\mu^2}{2} \left[ t\sqrt{t^2 - 1} + \ln(t + \sqrt{t^2 - 1}) \right]. \end{aligned} \quad (\text{B9})$$

Note also that these notations also allow to establish a link between the used here Darwin's expansion [43] and

the expansions of the Weber parabolic cylinder functions obtained in [52] (see also [53]).

Substituting the representations (B6) in Eq. (B1), where  $X^{-1/2}(\mathbf{a} + \lambda, x)$  and  $\theta(\mathbf{a} + \lambda, x)$  given by the expansions (B7) are rewritten using Eq. (B9), we arrive at very simple equation for unknown  $t$ :

$$\sqrt{-\mathbf{a}} = \gamma \kappa_-(t + \sqrt{t^2 - 1}). \quad (\text{B10})$$

Taking into account that for  $\delta = 0$  the parameter  $\kappa_- = \mu/\sqrt{2}$  the last equation reduces to

$$\gamma(t + \sqrt{t^2 - 1}) = 1, \quad (\text{B11})$$

which has a solution  $t = 1/\beta$ . Therefore, using the definition (B8) of  $t$  we find that  $\epsilon = \beta kl$  for  $kl \rightarrow -\infty$ .

- 
- [1] D.B. Chklovskii, B.I. Shklovskii, and L.I. Glazman, Phys. Rev. B **46**, 4026 (1992).
- [2] G. Li, A. Luican-Mayer, D. Abanin, L. Levitov, E.Y. Andrei, Nat. Commun **4**, 1744 (2013).
- [3] A. Coissard, A.G. Grushin, C. Repellin, L. Veyrat, K. Watanabe, T. Taniguchi, F. Gay, H. Courtois, H. Selier, and B. Sacépé, Preprint arXiv:2210.08152
- [4] G. Nazin, Y. Zhang, L. Zhang, E. Sutter, and P. Sutter, Nature Physics **6**, 870 (2010).
- [5] J.-P. Tetienne, N. Dontschuk, D. A. Broadway, A. Stacey, D. A. Simpson, and L. C. L. Hollenberg, Sci. Adv. **3**, e1602429 (2017).
- [6] S. Kim, J. Schwenk, D. Walkup, *et al.*, Nature Com. **12**, 2852 (2021).
- [7] A.H. MacDonald, Phys. Rev. B **28**, 2235 (1983).
- [8] M.M. Nieto and P.L. Taylor, Am. J. Phys. **53**, 234 (1985).
- [9] V. Lukose, R. Shankar, and G. Baskaran, Phys. Rev. Lett. **98**, 116802 (2007).
- [10] N.M.R. Peres and E.V. Castro, J. Phys.: Condens. Matter **19**, 406231 (2007).
- [11] V. Singh and M.M. Deshmukh Phys. Rev. B **80**, 081404(R) (2009).
- [12] N. Gu, M. Rudner, A.Young, P. Kim, and L. Levitov Phys. Rev. Lett. **106**, 066601 (2011).
- [13] P.M. Krstajić and P. Vasilopoulos, Phys. Rev. B **83**, 075427 (2011); Phys. Rev. B **86**, 079905 (2012).
- [14] E.V. Castro, M.A. Cazalilla, and M.A.H. Vozmediano, Phys. Rev. B **96**, 241405(R) (2017).
- [15] D. Grassano, M. D'Alessandro, O. Pulci, S.G. Sharapov, V.P. Gusynin, and A.A. Varlamov, Phys. Rev. B **101**, 245115 (2020).
- [16] P. Castro-Villarreal and R. Ruiz-Sánchez, Phys. Rev. B **95**, 125432 (2017).
- [17] P.A. Morales and P. Copinger, Phys. Rev. B **107**, 075432 (2023).
- [18] N. Levy, S.A. Burke, K.L. Meaker, M. Panlasigui, A. Zettl, F. Guinea, A.H.C. Neto, and M.F. Crommie, Science **329**, 544 (2010).
- [19] O. Roslyak, G. Gumbs, and D. Huang, Philos. Trans. R. Soc. London A **368**, 5431 (2010).
- [20] B. Ostahie, M. Niță, and A. Aldea Phys. Rev. B **91**, 155409 (2015).
- [21] Feng-Wu Chen, Nin-Yuan Lue, Mei-Yin Chou, Yu-Shu G. Wu, J. Appl. Phys. **132**, 164303 (2022).
- [22] A. Rycerz, J. Tworzydło, C.W.J. Beenakker, Nat. Phys. **3**, 172 (2007).
- [23] L. Z. Tan, C.-H. Park, and S. G. Louie, Phys. Rev. B **81**, 195426 (2009).
- [24] M. Milićević, G. Montambaux, T. Ozawa, O. Jamadi, B. Real, I. Sagnes, A. Lemaitre, L. Le Gratiet, A. Harouri, J. Bloch, and A. Amo, Phys. Rev. X **9**, 031010 (2019).
- [25] P. Somrooba, T. Sutthibutpong, S. Tangwancharoen, W. Liewriani, Physica E **127**, 114501 (2021).
- [26] D. E. Fernandes, Phys. Rev. B **107**, 085119 (2023).
- [27] L. Brey and H.A. Fertig, Phys. Rev. B **73**, 195408 (2006).
- [28] D.A. Abanin, P.A. Lee, and L.S. Levitov, Phys. Rev. Lett. **96**, 176803 (2006); Solid State Commun. **143**, 77 (2007).
- [29] I. Romanovsky, C. Yannouleas, and U. Landman, Phys. Rev. B **83**, 045421 (2011).
- [30] W. Wang and Z.S. Ma, Eur. Phys. J. B **81**, 431 (2011).
- [31] V.P. Gusynin, V.A. Miransky, S.G. Sharapov, and I.A. Shovkovy, Phys. Rev. B **77**, 205409 (2008).
- [32] V.P. Gusynin, V.A. Miransky, S.G. Sharapov, and I.A. Shovkovy, Fiz. Nizk. Temp. **34**, 993 (2008). [English transl. Low Temp. Phys. **34**, 778 (2008).]
- [33] V.P. Gusynin, V.A. Miransky, S.G. Sharapov, I.A. Shovkovy, and C.M. Wyenberg, Phys. Rev. B **79**, 115431 (2009).
- [34] P. Delplace, G. Montambaux, Phys. Rev. B **82**, 205412 (2010).
- [35] V.P. Gusynin, S.G. Sharapov, and J. P. Carbotte, Int. J. Mod. Phys. B **21**, 4611 (2007).
- [36] B. Hunt, J.D. Sanchez-Yamagishi, A.F. Young, M. Yankowitz, B.J. LeRoy, K. Watanabe, T. Taniguchi, P. Moon, M. Koshino, P. Jarillo-Herrero, and R.C. Ashoori, Science **340**, 1427 (2013).
- [37] R.V. Gorbachev, J.C.W. Song, G.L. Yu, A.V. Kretinin, F. Withers, Y. Cao, A. Mishchenko, I.V. Grigorieva, K.S. Novoselov, L.S. Levitov, and A.K. Geim, Science **346**, 448 (2014).
- [38] C.R. Woods, L. Britnell, A. Eckmann, R.S. Ma, J.C. Lu, H.M. Guo, X. Lin, G.L. Yu, Y. Cao, R.V. Gorbachev, A.V. Kretinin, J. Park, L.A. Ponomarenko, M.I. Kat-

- snelson, Yu.N. Gornostyrev, K. Watanabe, T. Taniguchi, C. Casiraghi, H.-J. Gao, A.K. Geim, and K. S. Novoselov, *Nat. Phys.* **10**, 451 (2014).
- [39] Z.-G. Chen, Z. Shi, W. Yang, X. Lu, Y. Lai, H. Yan, F. Wang, G. Zhang, and Z. Li, *Nat. Commun.* **5**, 4461 (2014).
- [40] E. McCann and V.I. Fal'ko, *J. Phys.: Condens. Matter* **16**, 2371 (2004).
- [41] L. Brey and H.A. Fertig, *Phys. Rev. B* **73**, 235411 (2006).
- [42] I.O. Nimyi, V. Könye, S.G. Sharapov, and V.P. Gusynin, *Phys. Rev. B* **106**, 085401 (2022).
- [43] M. Abramowitz and I. A. Stegun, *Handbook of Mathematical Functions With Formulas, Graphs, and Mathematical Tables* (U.S. GPO, Washington, D.C., 1972), p. 685.
- [44] Z.Z. Alisultanov, *Physica B* **438**, 41 (2014).
- [45] V. Arjona, E.V. Castro, and M.A.H. Vozmediano, *Phys. Rev. B* **96**, 081110(R) (2017).
- [46] M. Fujita, K. Wakabayashi, K. Nakada, and K. Kusakabe, *J. Phys. Soc. Jpn.* **65**, 1920 (1996).
- [47] M. Heuser and J. Hajdu, *Z. Physik* **270**, 289 (1974).
- [48] Yu. Yerin, V.P. Gusynin, S.G. Sharapov, and A.A. Varlamov, *Phys. Rev. B* **104**, 075415 (2021).
- [49] V. Galitski, B. Karnakov, V. Kogan and V. Galitski Jr., *Exploring Quantum Mechanics: A Collection of 700+ Solved Problems for Students, Lecturers, and Researchers* (Oxford University Press, 2013).
- [50] Y. Niimi, T. Matsui, H. Kambara, K. Tagami, M. Tsukada, and H. Fukuyama, *Phys. Rev. B* **73**, 085421 (2006).
- [51] S. Wu, B. Liu, C. Shen, S. Li, X. Huang, X. Lu, P. Chen, G. Wang, D. Wang, M. Liao, J. Zhang, T. Zhang, S. Wang, W. Yang, R. Yang, D. Shi, K. Watanabe, T. Taniguchi, Y. Yao, W. Wang, and G. Zhang, *Phys. Rev. Lett.* **120**, 216601 (2018).
- [52] N.M. Temme, *J. Comput. Appl. Math.* **121**, 221 (2000).
- [53] F.W. Olver, D.W. Lozier, R.F. Boisvert, and C.W. Clark, *NIST Handbook of Mathematical Functions Hardback and CD-ROM by National Institute of Standards and Technology (U.S.)* (Cambridge University Press, New York, 2010).